Type-II Dirac semimetal candidates ATe_2 (A = Pt, Pd): A de Haas-van Alphen study

Amit,[1] R. K. Singh,[1] Neha Wadehra,[2] S. Chakraverty,[2] and Yogesh Singh[1]

[1]*Department of Physical Sciences, Indian Institute of Science Education and Research Mohali, Sector 81, S. A. S. Nagar, Manauli, PO: 140306, India*

[2]*Nanoscale Physics and Laboratory, Institute of Nanoscience and Technology, SAS Nagar, Mohali, Punjab 140062, India*

(Received 13 June 2018; revised manuscript received 11 September 2018; published 13 November 2018)

We report on a magnetotransport and quantum oscillations study on high quality single crystals of the transition metal di-tellurides $PtTe_2$ and $PdTe_2$. The de Haas-van Alphen (dHvA) oscillations in the magnetization measurements on $PtTe_2$ reveal a complicated, anisotropic band structure characterized by low effective masses and high mobilities for the carriers. Extracted transport parameters for $PtTe_2$ reveal a strong anisotropy which might be related to the tilted nature of the Dirac cone. Using a Landau level fan diagram analysis we find at least one Fermi surface orbit with a Berry phase of π consistent with Dirac electrons for both $PtTe_2$ and $PdTe_2$. The light effective mass and high mobility are also consistent with Dirac electrons in $PtTe_2$. Our results therefore suggest that similar to $PdTe_2$, $PtTe_2$ might also be a three-dimensional Dirac semimetal.

DOI: 10.1103/PhysRevMaterials.2.114202

Recent discovery of topological semimetals (TSM) in three dimensions (3D), also known as 3D version of graphene, has intensified the search for this unique state of matter in various magnetic and nonmagnetic stoichiometric materials [1–5]. Graphene is considered topologically trivial due to an even number of band crossings at the Fermi level. Graphene can be gapped or localized by disorder. On the other hand, Dirac/Weyl semimetals (DSM/WSM) belong to the topological class of metals having an odd number of bulk bands with a linear dispersion in all three-momentum directions and are protected from gapping by certain symmetries [5–12]. A DSM can be transformed into a WSM by breaking time reversal symmetry, inversion symmetry, or both. Near the bulk Dirac point the low energy excitations mimic the relativistic massless quasiparticles predicted theoretically in the context of high energy physics. TSMs have been shown to exhibit exotic physical properties like the chiral anomaly, non-Ohmic transport, nonlocal conduction, a Berry phase of π, and many other anomalous optical and transport phenomena. Two forms of TSMs have been predicted theoretically, depending on the nature of the bulk Dirac dispersion relation. They are categorized as type-I and type-II TSMs. While type-I has linear and isotropic dispersion in the momentum space, the dispersion relation in the type-II topological semimetals is tilted.

The linear Dirac dispersion in the bulk band structure can be probed by studying quantum oscillations in transport experiments as has been demonstrated for graphene, topological insulators, and recently in the Dirac and Weyl semimetals [2]. Previous quantum oscillation studies on Weyl and Dirac semimetals have demonstrated a connection between band topology and the phase acquired by the charge carriers. The wave function of a relativistic quasiparticle acquires a nontrivial geometric phase of π along the cyclotron orbits in a magnetic field (also known as the π Berry phase), which can be calculated from the quantum oscillations in resistivity and magnetization [2].

The tilting of the Dirac cone has been predicted in $PtTe_2$ and $PdTe_2$ as well [13–20]. $PdTe_2$ has previously been confirmed to be a Dirac semimetal by angle resolved photoemission and quantum oscillation experiments [15,17,18,21–24]. In the transition metal di-telluride family experimental work focusing on demonstrating the type-II DSM nature has been mainly on $PdTe_2$, $PtSe_2$, and Pd/PtSeTe compounds [14,19,21,25]. However, experimental evidence for the DSM nature of another compound from the same family $PtTe_2$ is missing. There are some photoemission spectroscopy reports regarding tilted nature of the Dirac cone in $PtTe_2$, but quantum oscillation studies on this compound are still missing, which can help establish the three-dimensional Dirac character of this compound. The key signatures of Dirac carriers, such as low (ideally massless) effective mass of carriers, high mobility, and a Berry phase of π can be extracted from quantum oscillation measurements [10–12,26–31].

In this article we have measured dHvA quantum oscillations on high quality single crystals of $PtTe_2$ and $PdTe_2$ for both out-of-plane ($B\|c$) and in-plane ($B\|ab$) configurations. The temperature dependent resistivity measurements reveal a typical metallic character with high residual resistivity ratio (RRR) for the two cases. The RRR for $PdTe_2$ is $\approx$238 and that for $PtTe_2$ is $\approx$96. Both $PtTe_2$ and $PdTe_2$ show pronounced magnetization quantum oscillations with multiple frequencies which suggests multiple Fermi pockets crossing the Fermi level. The number and positions of the frequencies suggest different band structures for $PdTe_2$ and $PtTe_2$. For the orbit with the largest amplitude, the extracted Berry phase is close to the value π for both $PtTe_2$ and $PdTe_2$. The analysis of the observed quantum oscillations in both in-plane and out-of-plane field orientations enables us to calculate important band parameters for the two semimetals. Low effective masses and high mobilities are estimated for both materials. Additionally, a Berry phase close to π for at least one orbit strongly suggests the Dirac nature of bulk carriers in these two Dirac semimetals.

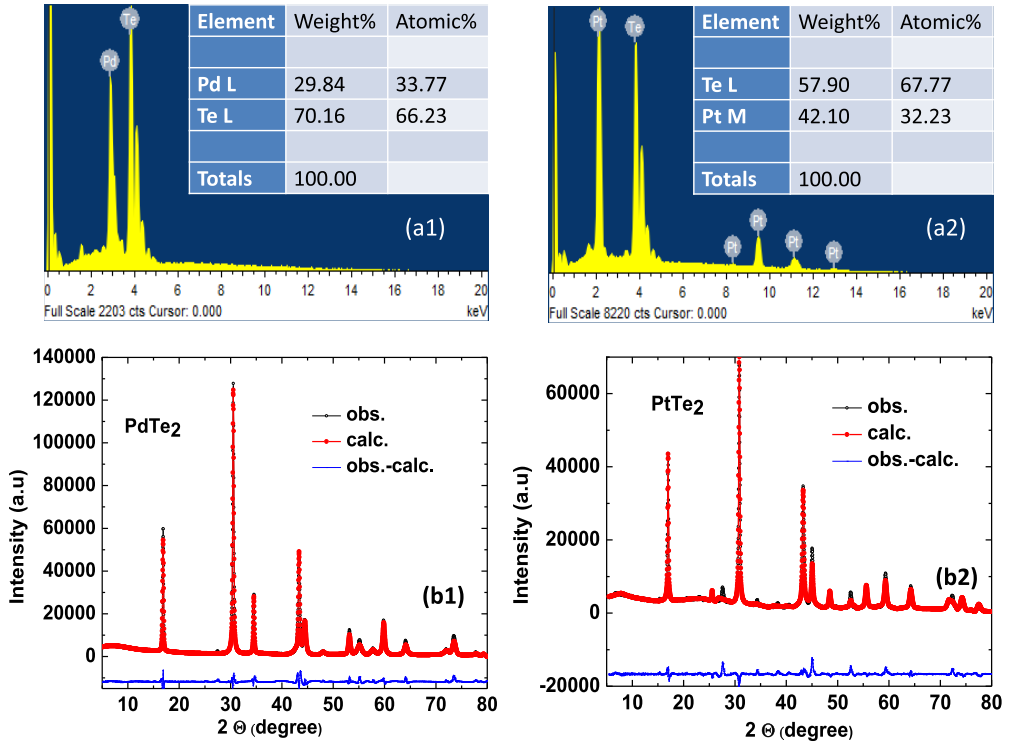

FIG. 1. Results of chemical analysis (a1) and (a2) and powder x-ray diffraction (b1) and (b2) on $PdTe_2$ and $PtTe_2$, respectively.

I. EXPERIMENT

High quality single crystals of $PdTe_2$ were synthesized by a modified Bridgman technique as reported earlier [32]. For $PtTe_2$ crystals, the starting elements Pt powder (99.9 %, Alfa Aesar) and Te lump (99.9999%, Alfa Aesar) were taken in the molar ratio 2 : 98 and sealed in an evacuated quartz tube. The tube was heated to 790°C in 15 h, kept at this temperature for 48 h in order to homogenize the solution, and then slowly cooled to 500°C at a rate of 2.5°C/h. The excess Te liquid was decanted isothermally for 2 days. Finally, the tube was allowed to cool down to room temperature by shutting off the furnace. Platelike hexagonal shaped crystals were obtained after breaking open the tube at room temperature. A typical crystal of $PtTe_2$ is shown on a millimeter grid in the inset of Fig. 2. The powder x-ray diffraction pattern obtained on crushed crystals of $PdTe_2$ and $PtTe_2$ confirms the phase purity and CdI2 type crystal structure with $P3m1$ (No. 164) space group for both materials. The chemical composition and uniformity of stoichiometry for crystals of both compounds was confirmed by energy dispersive spectroscopy at several spots on the crystals used for the measurements reported in this work. The results of chemical analysis and powder x-ray diffraction for ATe_2 are shown in Fig. 1. The electrical transport and magnetic measurements (0–14 T) were performed on a physical property measurement system by Quantum Design (QD-PPMS).

II. RESULTS

A. $PtTe_2$

Figure 2 shows electrical resistivity ρ versus temperature T for a single crystal of $PtTe_2$ measured with an ac current of amplitude $I = 2$ mA applied within the ab plane of the crystal. Metallic behavior is observed in the whole T range (1.8 to 300 K) of measurements. The residual resistivity ratio $\mathrm{RRR} = \rho(300\ \mathrm{K})/\rho(1.8\ \mathrm{K}) \approx 96$ indicates the high quality of the crystal. The top inset shows an optical image of an as-grown $PtTe_2$ crystal showing the hexagonal morphology of the underlying crystal structure. The bottom inset shows the electrical resistance R vs T for a crystal of $PdTe_2$. The RRR for this $PdTe_2$ crystal was ≈238. A high RRR has been regarded as an indication of relativistic charge carriers in

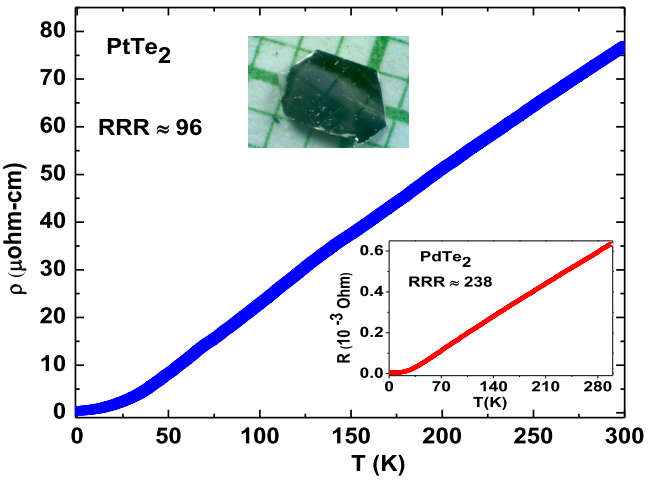

FIG. 2. Temperature dependent electrical resistivity of $PtTe_2$ and $PdTe_2$ (lower inset) single crystals. A current $I = 2$ mA is applied in the crystallographic ab plane. Upper inset shows an optical image of a $PtTe_2$ crystal placed on a millimeter grid.

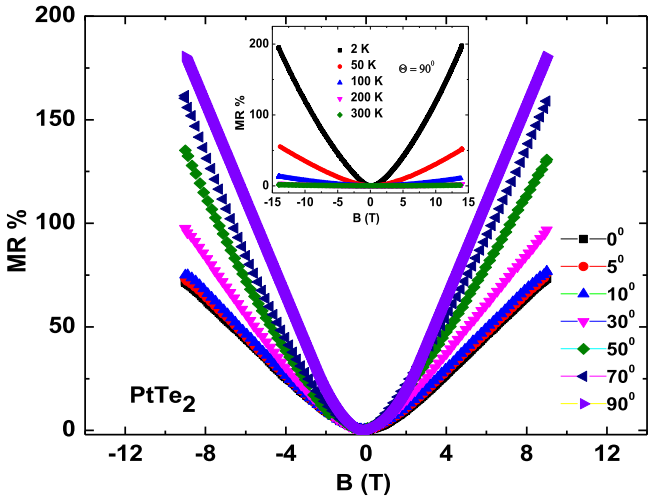

FIG. 3. Magnetoresistance (MR) for $PtTe_2$ as a function of the magnetic field $B \leqslant 9$ T applied at various angles to the direction of the current I which was always applied within the ab plane. Inset shows the MR measured at various T with $B \perp I$ for $B \leqslant 14$ T.

three-dimensional Dirac semimetals such as Cd_3As_2, NbAs, $PdTe_2$, and NbP among others [17,26–28,31–35].

Figure 3 shows the magnetoresistance (MR) data on the $PtTe_2$ crystal. The main panel shows the magnetic field B dependence of the MR measured at $T = 2$ K as a function of the angle between $B \leqslant 9$ T and the direction of the electrical current I, which was always applied in the same direction within the ab plane of the crystal. The MR for all angles increases monotonically and tends to a linear in B behavior. The magnitude of MR reaches about 200% which is smaller than observed for other DSMs. We specifically point out that no negative contribution to the MR was observed for $B \| I$ indicating the absence of the Chiral anomaly. The MR as a function of $B \perp I$ at various temperatures T is shown in the inset of Fig. 3 and shows that the magnitude of MR has a strong T dependence.

The isothermal magnetization M data for $PtTe_2$ plotted as dM/dB versus $1/B$ at different temperatures for magnetic fields $B \leqslant 14$ T applied along the c axis ($B \| c$) and applied within the ab plane ($B \| ab$) are shown in Figs. 4(a1) and 4(a2), respectively. The raw M vs B data for the two field directions are shown in the insets. The magnetization data reveal pronounced dHvA oscillations starting from 4 T. The low onset field value of the quantum oscillations also point to the high quality of the $PtTe_2$ crystal. Pronounced periodic oscillations as a function of $1/B$ are clearly visible up to 10 K in both field orientations. Multiple frequencies for both field orientations were observed in the fast Fourier transform (FFT) spectra of the quantum oscillations as shown in Figs. 4(b1) and 4(b2). The multiple frequencies in the FFT spectra indicates the presence of multiple Fermi surface pockets at the Fermi level. Additionally, the presence of dHvA oscillations for both $B \| c$ and $B \| ab$ directions, confirms the presence of a three-dimensional Fermi surface in $PtTe_2$. From the temperature dependent FFT spectra, we identify four main frequencies for both $B \| c$ and $B \| ab$ as shown in Figs. 4(b1) and 4(b2). The main frequencies for the $B \| c$ are labeled as α_1(93.3 T), α_2(108.9 T), α_3(241 T), and α_4(459 T). The main frequencies for $B \| ab$ are labeled β_1(116.6 T), β_2(140.6 T), β_3(194.5 T), and β_4(225.6 T). The information regarding

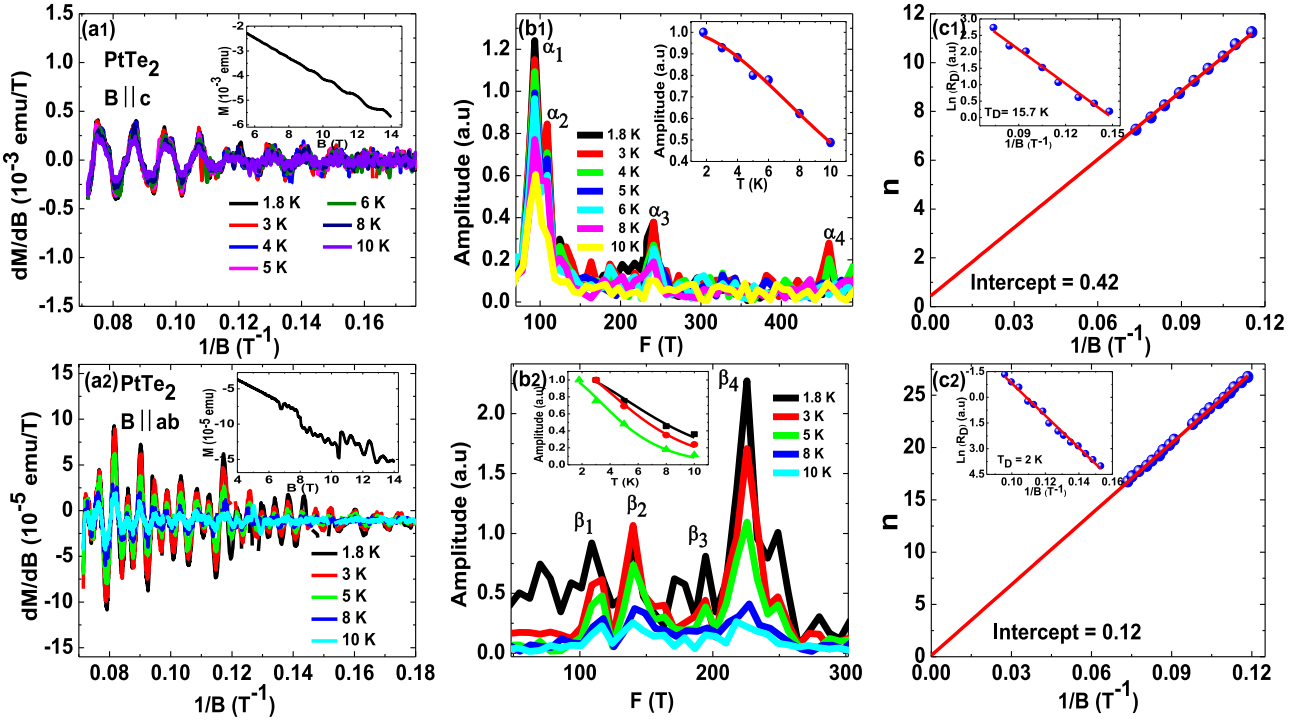

FIG. 4. (a1) and (a2) Isothermal magnetization oscillation data for $PtTe_2$ in the two directions $B \| c$ and $B \| ab$, at various temperatures. Inset shows row magnetization data at 1.8 K. (b1) and (b2) The temperature dependence of FFT spectra and fitting of the temperature dependent amplitude is shown in the inset for the two cases. (c1) and (c2) The Landau level fan diagrams for the two cases. Inset shows the Dingle fitting.

TABLE I. Fermi surface parameters for $PtTe_2$ obtained from the dHvA data shown in Figs. 4(b1) and 4(b2).

Compound	F (T)	A_f (Å^{-2}) (10^{-2})	K_f (Å^{-1}) (10^{-2})	m^*/m	v_f (m/s) (10^5)	E_f (meV)
$PtTe_2$, $B\|\|c$	93.3	0.89	5.3	0.15 ± 0.004	4.1 ± 0.1	143 ± 5
	108.9	1	5.7	–	–	–
	241	2.3	8.6	–	–	–
	459	4.4	11.8	–	–	–
$PtTe_2$, $B\|\|ab$	116.6	1.1	5.96	0.21 ± 0.01	3.3 ± 0.2	128 ± 9
	140.6	1.3	6.54	0.26 ± 0.01	2.9 ± 0.1	124 ± 9
	194.5	1.9	7.7	–	–	–
	225.6	2.1	8.3	0.32 ± 0.01	3 ± 0.1	164 ± 11

the Fermi surface area corresponding to these frequencies can be determined by the Onsager relation $F = A_F(\varphi/2\pi^2)$, where $\varphi = h/e$ is the magnetic flux quantum and A_F is the Fermi surface area. The calculated Fermi surface area for the frequencies extracted for the two field orientations are listed in Table I.

A quantitative analysis of the dHvA oscillations can be made using the Lifshitz-Kosevich (LK) equation which gives the oscillatory contribution to the magnetization as

$$\Delta M \propto -R_T R_D \sin\left\{2\pi\left[\frac{F}{B} - \left(\frac{1}{2} - \phi\right)\right]\right\}, \qquad (1)$$

where $R_D = \exp(-\lambda T_D)$ is the Dingle factor, $T_D = \hbar/2\pi K_B \tau$ is the Dingle temperature, and the temperature dependent damping of the oscillations is accounted for by the factor $R_T = \lambda T/\sinh(\lambda T)$, with $\lambda = (2\pi^2 K_B m^*/\hbar e B)$ and m^* the effective cyclotron mass. The phase $\phi = \phi_B/2\pi - \delta$, where ϕ_B is the Berry phase and δ is an extra phase factor. The value of this additional phase shift δ depends on the dimensionality of the Fermi surface and takes the value 0 or $\pm 1/8$ ($-$ for electronlike and $+$ for the holelike) for two and three dimension, respectively [27–29,37].

The damping factors R_T and R_D can be used to calculate important band parameters such as m^*, carrier lifetime τ, and quantum mobility μ of the carriers. The τ and μ here are different from transport relaxation time and transport mobility. The transport relaxation time is a measure of the average time an electron moves without changing the direction of its momentum. On the other hand, the carrier lifetime is the average time an electron stays in a given quantum state. The transport scattering time can be calculated from Hall mobility, and carrier lifetime from quantum oscillations at quantizing magnetic fields. In our paper we calculated mobility and lifetime by using dHvA oscillations. So τ is carrier lifetime and μ is the quantum mobility.

The values of τ (corresponding to Dingle temperature T_D) extracted from fitting of the B dependence [see inset of Figs. 4(c1) and 4(c2)] of the oscillation amplitude are given in the Table II. For $B\|c$ the value of $\tau = 7.7 \times 10^{-14}$ s, and for $B\|ab$, $\tau = 6.0 \times 10^{-13}$ s. The corresponding quantum mobility $\mu = e\tau/m^*$ in the two directions are estimated to be 902.0 and 3296 cm^2/V s, respectively. These values of μ are comparable to values reported previously for some topological semimetals like Na_3Bi and GdPtBi but are much smaller than the values reported for Cd_3As_2 and NbP [21,28,29,36,37]. The large difference in the mobility (more than a factor of 3) in the two crystal orientations suggests that the dynamics of carriers in $PtTe_2$ is highly anisotropic with carriers in the c-axis direction being less mobile than in the ab plane. This anisotropy can arise from an anisotropic Fermi surface as expected for layered materials. However, the anisotropy might also have contributions from the predicted tilted Dirac cone in $PtTe_2$.

The value of the effective mass for the two field orientations is found from fitting the temperature dependence of the amplitudes of frequencies identified in the FFT spectra of the dHvA oscillations. The fitting shown in the insets of Figs. 4(b1) and 4(b2) was successful only for certain frequencies as the amplitude dropped too rapidly with T for some frequencies. The effective masses thus obtained are listed in the Table I. For $B\|c$ the value of the effective mass m^* corresponding to the frequency $\alpha_1 = 93.3$ T is 0.15. The low value of m^* for this frequency suggests the presence of relativistic charge carriers. The Landau level fan diagram analysis which we present later is also consistent with this inference. The values of m^* corresponding to frequencies in the $B\|ab$ orientation are relatively larger in magnitude as listed in Table I.

We now present a Landau fan diagram analysis to estimate the Berry phase. The presence of multiple frequencies (from multiple Fermi surface orbits) in the quantum oscillations makes it difficult to isolate contributions to the Berry phase from individual orbits. We therefore take into account the frequencies with the largest FFT amplitudes ($\alpha_1 = 93.3$ T for the $B\|c$ and $\beta_4 = 225.6$ T in case of $B\|ab$) as shown in the Figs. 4(b1) and 4(b2). To construct the Landau level fan diagram we assign the Landau index $n - 1/4$ to the minima of quantum oscillations. We are able to reach the seventh Landau level in the $B\|c$ and 16th Landau level for the $B\|ab$ configuration as shown in the Figs. 4(c1) and 4(c2). The extrapolated value of the intercept ($=\phi_B/2\pi \pm \delta$) on the n axis is found to be 0.42(2) and 0.12(1) for $B\|c$ and $B\|ab$, respectively. The slopes obtained from the fits are 94.7 and 228.2 T for the two directions. These slopes are very close to the frequencies of the α_1 and β_4 orbits, proving that we are

TABLE II. Parameters obtained from a Dingle fitting of the dHvA data shown in Fig. 4.

Compound	T_D (K)	τ (10^{-13} s)	l (nm)	μ (cm^2/V s)
$PtTe_2$, $B\|\|c$	16 ± 1	0.77 ± 0.06	32 ± 4	902 ± 87
$PtTe_2$, $B\|\|ab$	2 ± 0.1	6 ± 0.4	180 ± 21	3296 ± 386

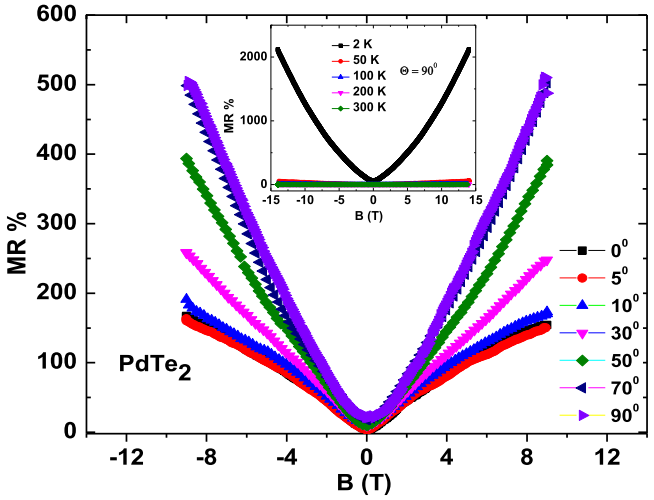

FIG. 5. Magnetoresistance (MR) for a $PdTe_2$ single crystal as a function of the magnetic field $B \leqslant 9$ T applied at various angles to the direction of the current I which was always applied within the ab plane. Inset shows the MR measured at various T with $B \perp I$ for $B \leqslant 14$ T.

primarily analyzing these orbits in the Landau level fan diagram [2]. From the value of the intercepts found above the estimated Berry phase for $B \| c$ and $B \| ab$ directions are $1.08(4)\pi$ [or $0.59(4)\pi$] and $0.49(2)\pi$ [or $-0.01(2)\pi$], respectively. The value $\phi_B = 1.08(4)\pi$ for the α_1 orbit in $B \| c$ direction is very close to the value π expected for Dirac electrons. Whereas the value $\phi_B = 0$ for $B \| ab$ suggests that the orbit β_4 is trivial. A possible reason for the trivial character of bands in the $B \| ab$ direction can be the nonlinear nature of the bands owing to the Fermi level being away from the Dirac point. We will discuss the validity of these numbers in our discussion section later.

B. $PdTe_2$

To be able to make a comparison between the two materials we have performed similar magnetotransport measurements and analysis on $PdTe_2$ single crystals. Figure 5 shows the magnetoresistance (MR) data on a $PdTe_2$ crystal for which $B = 0$ electrical resistivity was shown in the lower inset of Fig. 2. The main panel in Fig. 5 shows the magnetic field dependence of the MR measured at $T = 2$ K as a function of the angle between $B \leqslant 9$ T and the direction of the electrical current I, which was always applied in the same direction within the ab plane of the crystal. The MR for all angles increases monotonically with B. The magnitude of MR reaches large values of about 600% for $B \perp I$. As for $PtTe_2$, no negative contribution to the MR was observed for $B \| I$ indicating the absence of the Chiral anomaly. The MR as a function of $B \perp I$ at various temperatures T is shown in the inset of Fig. 3 and shows that the magnitude of MR has a very strong T dependence dropping drastically as one increases T from 2 K.

Figure 6 shows the magnetic field dependence of the magnetization data for $PdTe_2$ for both $B \| c$ and $B \| ab$ directions, measured at different temperatures. Figures 6(a1) and 6(a2)

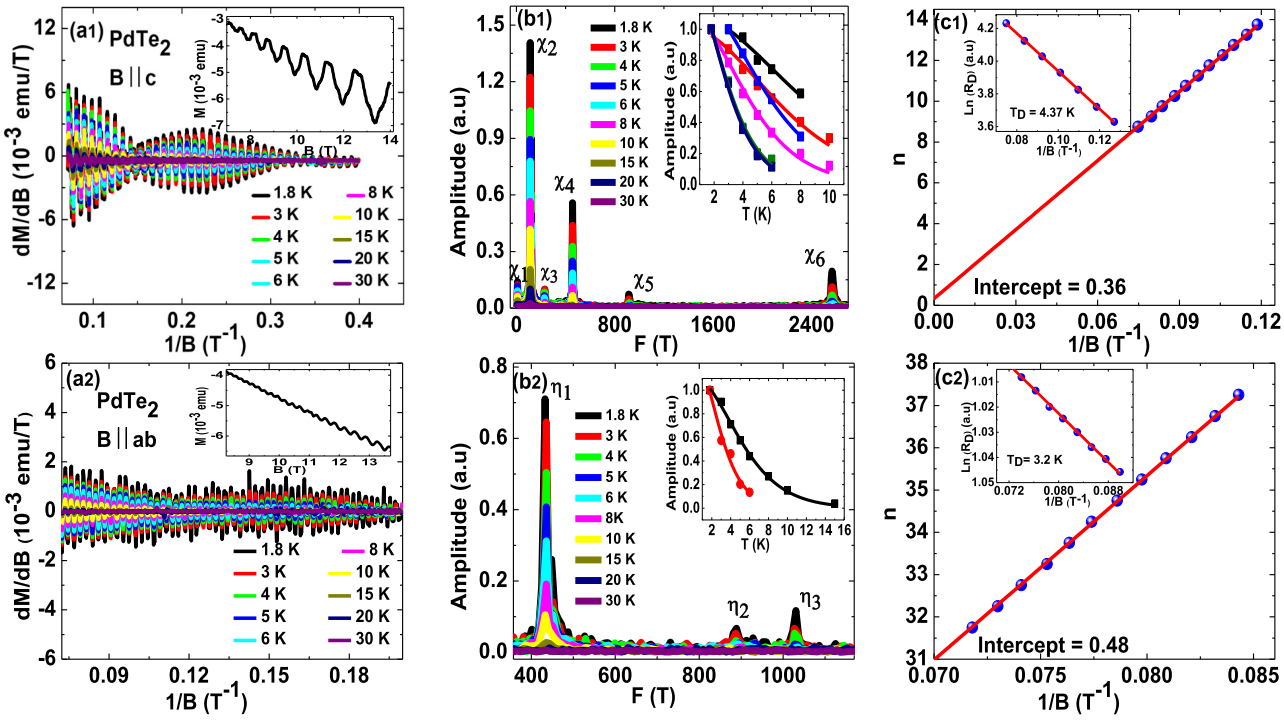

FIG. 6. (a1) and (a2) Similar set of magnetization data for $PdTe_2$. Magnetization oscillation data for $PdTe_2$ in the two directions $B \| c$ and $B \| ab$, at various temperatures. Inset shows row magnetization data at 1.8 K. (b1) and (b2) The temperature dependence of FFT spectra and fitting of the temperature dependent amplitude is shown in the inset for the two cases. (c1) and (c2) The Landau level fan diagrams for the two cases. Inset shows the Dingle fitting.

TABLE III. Fermi surface parameters for $PdTe_2$ obtained from the dHvA frequencies shown in Figs. 6(b1) and 6(b2).

Compound	F (T)	A_f (Å^{-2}) (10^{-2})	K_f (Å^{-1}) (10^{-2})	m^*/m	v_f (m/s) (10^5)	E_f (meV)
$PdTe_2$, $B\|c$	9.13	0.087	1.7	0.14 ± 0.01	1.4 ± 0.1	16 ± 1
	112.7	1.1	5.84	0.18 ± 0.01	3.7 ± 0.1	140 ± 7
	228.7	2.2	8.4	0.22 ± 0.01	4.4 ± 0.2	242 ± 15
	456.9	4.37	11.8	0.27 ± 0.01	5 ± 0.2	383 ± 19
	913.9	8.75	16.7	0.41 ± 0.01	4.7 ± 0.2	514 ± 27
	2568	24.6	28	0.43 ± 0.02	7.5 ± 0.3	1374 ± 73
$PdTe_2$, $B\|ab$	435.8	4.17	6.5	0.26 ± 0.01	2.9 ± 0.1	124 ± 7
	889	8.5	16.5	–	–	–
	1035.5	9.8	17.7	0.46 ± 0.02	4.4 ± 0.2	506 ± 32

show the pronounced dHvA oscillations for both directions of magnetic field. It should be noted that the amplitude of the quantum oscillations in $PdTe_2$ is relatively larger than in $PtTe_2$ single crystals and persist up to a temperature more than 30 K. The presence of the multiple frequencies in the two field orientations indicates an even more complex bulk band structure for $PdTe_2$ consisting of multiple Fermi pockets at the Fermi level. The FFT of the oscillations are shown in Figs. 6(b1) and 6(b2) and reveal six main frequencies for $B\|c$ which we label as χ_1(9.13 T), χ_2(112.7 T), χ_3(231.5 T), χ_4(456.9 T), χ_5(913.9 T), and χ_6(2568 T), and three major frequencies for $B\|ab$ which we label as η_1(435.8 T), η_2(889 T), and η_3(1030.5 T), respectively. The calculated effective masses for the different frequencies for $B\|c$ are listed in Table III and lie in the range 0.14–0.43. The value of the cross-sectional area calculated using the Onsager relation for the lowest effective mass Fermi orbit χ_1 comes out to be 0.87×10^{-3}, which is very small compared to the area for other orbits observed for $B\|c$. The value of the lowest effective mass for the $B\|ab$ direction is found to be 0.26 which is higher than estimated for $B\|c$ direction. Despite the difference in the effective masses in the two directions, the mobility calculated from a Dingle fitting for the two directions are very similar as shown in Table IV, in sharp contrast to the case of $PtTe_2$. These results are consistent with a recent magnetization and ARPES study on $PdTe_2$ single crystals [17].

The Landau level fan diagrams for the two directions are given in Figs. 6(c1) and 6(c2). The intercepts are 0.36(2) and 0.48(2) for $B\|c$ and $B\|ab$, respectively. The corresponding values of the Berry phase are $\phi_B = 0.97(4)\pi$ [or $0.47(4)\pi$] and $1.21(4)\pi$ [or $0.71(4)\pi$] for $B\|c$ and $B\|ab$. The value ϕ_B for $B\|c$ is very close to π while the Berry phase for $B\|ab$ deviates from π. We note that the Fermi level in $PdTe_2$, like in $PtTe_2$, is located away from the 3D Dirac point as observed in ARPES measurements [17,18,20,21].

TABLE IV. Parameters obtained from a Dingle fitting to the dHvA data shown in Fig. 6.

Compound	T_D (K)	τ (10^{-13} s)	l (nm)	μ (cm^2/V s)
$PdTe_2$, $B\|c$	4.4 ± 0.2	2.8 ± 0.1	104 ± 8	2735 ± 112
$PdTe_2$, $B\|ab$	3.2 ± 0.2	3.8 ± 0.2	110 ± 10	2570 ± 234

III. DISCUSSION AND CONCLUSION

We have presented a detailed magnetotransport study on single crystals of the di-tellurides $PtTe_2$ and $PdTe_2$ with an emphasis on trying to ascertain the possible topological nature of the bands contributing to the transport. Prominent dHvA quantum oscillations are observed for both materials in both directions of applied magnetic fields. From an analysis of the magnetization data on the two materials, it is found that the Fermi surface of both systems is highly anisotropic in nature which is evident from the different number of oscillation frequencies in the two field directions. Additionally for $PtTe_2$ a very large difference in the value of the mobility (more than three times) in the two crystal orientations is observed and would be consistent with expectations of highly anisotropic transport resulting from the tilted nature of the Dirac cone in the $PtTe_2$. The Berry phase for $PtTe_2$ is close to π for $B\|c$ while it deviates from π for $B\|ab$. We speculate that this could be due to a combination of the Fermi level being away from the Dirac point and the presence of other topologically trivial bands at the Fermi level. This anisotropy is almost absent in case of $PdTe_2$ as the calculated mobility in the two crystal orientations is of the same magnitude. The bands in $PdTe_2$ are indeed three-dimensional Dirac bands characterized by a Berry phase close to π in both in-plane and out-of-plane crystal orientations.

A word of caution is in order here. An unambiguous identification of the Berry phase from quantum oscillations is complicated for systems with multiple bands making up the Fermi surface resulting in multiple frequencies in the oscillation data. Each frequency will contribute to the phase. The analysis is further complicated if the Dirac node sits away from the Fermi energy. Additionally, if one ends up with a large Landau band index n in the Landau fan diagram analysis, then a larger extrapolation is required to reach the quantum limit to determine the intercept and hence the phase. This results in a larger error in the phase. For the ATe_2 materials, all these difficulties are present.

We have tried to circumvent the problem of multiple frequencies by analyzing the frequency with the largest amplitude in the FFT data. The validity of this approach is confirmed after the fact, when the slope in the Landau fan diagram equals the frequency of the band we used to construct the Landau fan diagram. For $PtTe_2$ we chose the frequencies $\alpha_1 = 93.3$ T for the $B\|c$ and $\beta_4 = 225.6$ T in case of $B\|ab$.

The slopes obtained from the fits of the Landau fan diagram are 94.7 and 228.2 T for the two directions. These values are very close to the frequencies for α_1 and β_4 and hence validates our approach above.

We have estimated the Berry phase ϕ_B close to π for both $PtTe_2$ and $PdTe_2$ when $B\|c$. We point out that the Landau index n for these two cases is 7 and 8, respectively, which is a reasonably small index. Therefore we believe that the extrapolation to estimate the intercept can be trusted. Measurements at lower temperatures and higher magnetic fields are desirable to reach even smaller Landau index so that the extrapolation to the quantum limit has an even smaller error. We note that for $PdTe_2$ there have been SdH measurements at $T = 1.7$ K for $B||c$ with fields up to 35 T and a Landau fan diagram was constructed which reached $n = 1$ [17]. This study estimated a Berry phase of π from these measurements which is consistent with what we conclude from our data even though we start from a larger n. This gives us confidence that even for $PtTe_2$, our conclusion of $\phi_B \approx \pi$ could be valid although future experiments in higher fields can be used to confirm these results.

Our results therefore suggest that $PtTe_2$ like $PdTe_2$, could also be a type-II Dirac semimetal.

Note added. While this manuscript was under preparation another quantum oscillation study on ATe_2 (A = Pt, Pd) has appeared on the arXiv [38]. This work also reports low carrier effective masses and high mobilities for the two materials. Their Landau level fan diagram analysis however, is different. In order to obtain the contribution from an individual orbit out of the multifrequency quantum oscillation data, they have used a low-pass filter of 50 T to get the contribution from the lowest frequency orbit 8 T for $PdTe_2$ in the $B\|c$ direction. From the Landau level fan diagram obtained from this they conclude that the Berry phase for this orbit is different from π.

We point out that by applying a low-pass filter, one cannot get a unique Landau level diagram as the location of the maxima and minima in the oscillation data obtained after applying the filter depend on what kind of filter has been applied. In Fig. 7 we show the result of applying different low-pass filters to the dHvA data for $PdTe_2$ for $B\|c$. It is clear that different filters give oscillations with slightly different locations of the maxima and minima, which are used to construct the Landau level fan diagram. This suggests that the Landau fan diagram and any numbers obtained from an analysis of the same will strongly depend on the filter applied.

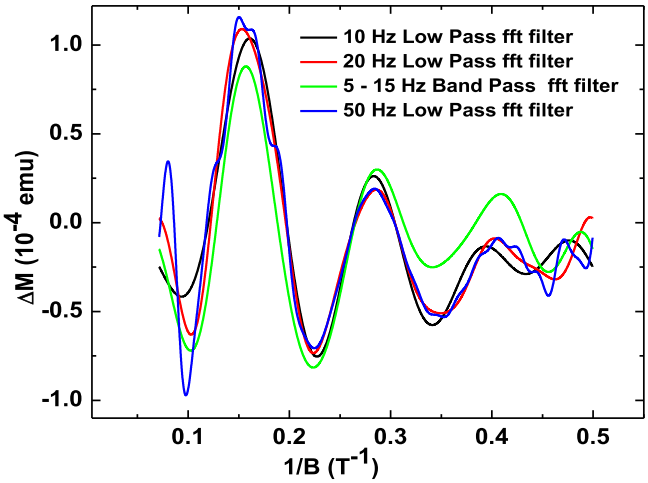

FIG. 7. Oscillatory signal obtained after applying various low-pass filters to the dHvA data for $PdTe_2$ in the $B\|c$ direction. The positions of the extrema in oscillations clearly depend on what filter is applied.

ACKNOWLEDGMENTS

We acknowledge use of the XRD and SEM central facilities at IISER Mohali. S.C. and N.W. would like to acknowledge financial support from Department of Science and Technology (DST) India, Nano Mission Project No. SR/NM/NS-1007/2015.

[1] M. Z. Hasan and C. L. Kane, Rev. Mod. Phys. **82**, 3045 (2010).
[2] Y. Ando, J. Phys. Soc. Jpn. **82**, 102001 (2013).
[3] X.-L. Qi and S.-C. Zhang, Rev. Mod. Phys. **83**, 1057 (2011).
[4] S. M. Young, S. Zaheer, J. C. Y. Teo, C. L. Kane, E. J. Mele, and A. M. Rappe, Phys. Rev. Lett. **108**, 140405 (2012).
[5] A. A. Zyuzin and A. A. Burkov, Phys. Rev. B **86**, 115133 (2012).
[6] F. Wilczek, Phys. Today **51**(1), 11 (1998).
[7] S.-Y. Xu, I. Belopolski, N. Alidoust, M. Neupane, G. Bian, C. Zhang, R. Sankar, G. Chang, Z. Yuan, C.-C. Lee, S.-M. Huang, H. Zheng, J. Ma, D. S. Sanchez, B. Wang, A. Bansil, F. Chou, P. P. Shibayev, H. Lin, S. Jia, and M. Z. Hasan, Science **349**, 613 (2015).
[8] A. A. Soluyanov, D. Gresch, Z. Wang, Q. Wu, M. Troyer, X. Dai, and B. A. Bernevig, Nature (London) **527**, 495 (2015).
[9] Z. K. Liu, B. Zhou, Y. Zhang, Z. J. Wang, H. M. Weng, D. Prabhakaran, S.-K. Mo, Z. X. Shen, Z. Fang, X. Dai, Z. Hussain, and Y. L. Chen, Science **343**, 864 (2014).
[10] S.-Y. Xu, C. Liu, S. K. Kushwaha, R. Sankar, J. W. Krizan, I. Belopolski, M. Neupane, G. Bian, N. Alidoust, T.-R. Chang, H.-T. Jeng, C.-Y. Huang, W.-F. Tsai, H. Lin, P. P. Shibayev, F.-C. Chou, R. J. Cava, and M. Z. Hasan, Science **347**, 294 (2015).
[11] Z. K. Liu, J. Jiang, B. Zhou, Z. J. Wang, Y. Zhang, H. M. Weng, D. Prabhakaran, S.-K. Mo, H. Peng, P. Dudin, T. Kim, M. Hoesch, Z. Fang, X. Dai, Z. X. Shen, D. L. Feng, Z. Hussain, and Y. L. Chen, Nat. Mater. **13**, 677 (2014).
[12] M. Neupane, S.-Y. Xu, R. Sankar, N. Alidoust, G. Bian, C. Liu, I. Belopolski, T.-R. Chang, H.-T. Jeng, H. Lin, A. Bansil, F. Chou, and M. Z. Hasan, Nat. Commun. **5**, 3786 (2014).
[13] A. A. Burkov, Nat. Mater. **15**, 1145 (2016).
[14] R. C. Xiao, C. H. Cheung, P. L. Gong, W. J. Lu, J. G. Si, and Y. P. Sun, J. Phys.: Condens. Matter **30**, 245502 (2018).
[15] R. C. Xiao, P. L. Gong, Q. S. Wu, W. J. Lu, M. J. Wei, J. Y. Li, H. Y. Lv, X. Luo, P. Tong, X. B. Zhu, and Y. P. Sun, Phys. Rev. B **96**, 075101 (2017).
[16] S. Teknowijoyo, N. H. Jo, M. S. Scheurer, M. A. Tanatar, K. Cho, S. L. Bud'ko, P. P. Orth, P. C. Canfield, and R. Prozorov, Phys. Rev. B **98**, 024508 (2018).

[17] F. Fei, X. Bo, R. Wang, B. Wu, J. Jiang, D. Fu, M. Gao, H. Zheng, Y. Chen, X. Wang, H. Bu, F. Song, X. Wan, B. Wang, and G. Wang, Phys. Rev. B **96**, 041201 (2017).
[18] H.-J. Noh, J. Jeong, E.-J. Cho, K. Kim, B. I. Min, and B.-G. Park, Phys. Rev. Lett. **119**, 016401 (2017).
[19] O. J. Clark *et al.*, Phys. Rev. Lett. **120**, 156401 (2018).
[20] M. Yan, H. Huang, K. Zhang, E. Wang, W. Yao, K. Deng, G. Wan, H. Zhang, M. Arita, H. Yang, Z. Sun, H. Yao, Y. Wu, S. Fan, W. Duan, and S. Zhou, Nat. Commun. **8**, 257 (2017).
[21] M. S. Bahramy, O. J. Clark, B.-J. Yang, J. Feng, L. Bawden, J. M. Riley, I. Markovic, F. Mazzola, V. Sunko, D. Biswas, S. P. Cooil, M. Jorge, J. W. Wells, M. Leandersson, T. Balasubramanian, J. Fujii, I. Vobornik, J. E. Rault, T. K. Kim, M. Hoesch, K. Okawa, M. Asakawa, T. Sasagawa, T. Eknapakul, W. Meevasana, and P. D. C. King, Nat. Mater. **17**, 21 (2017).
[22] S. Das, Amit, A. Sirohi, L. Yadav, S. Gayen, Y. Singh, and G. Sheet, Phys. Rev. B **97**, 014523 (2018).
[23] K. Zhang, M. Yan, H. Zhang, H. Huang, M. Arita, Z. Sun, W. Duan, Y. Wu, and S. Zhou, Phys. Rev. B **96**, 125102 (2017).
[24] H. Huang, S. Zhou, and W. Duan, Phys. Rev. B **94**, 121117 (2016).
[25] Y. Li, Y. Xia, S. A. Ekahana, N. Kumar, J. Jiang, L. Yang, C. Chen, C. Liu, B. Yan, C. Felser, G. Li, Z. Liu, and Y. Chen, Phys. Rev. Mater. **1**, 074202 (2017).
[26] S. Pezzini, M. R. van Delft, L. M. Schoop, B. V. Lotsch, A. Carrington, M. I. Katsnelson, N. E. Hussey, and S. Wiedmann, Nat. Phys. **14**, 178 (2017).
[27] N. Kumar, K. Manna, Y. Qi, S.-C. Wu, L. Wang, B. Yan, C. Felser, and C. Shekhar, Phys. Rev. B **95**, 121109 (2017).
[28] J. Hu, Z. Tang, J. Liu, X. Liu, Y. Zhu, D. Graf, K. Myhro, S. Tran, C. N. Lau, J. Wei, and Z. Mao, Phys. Rev. Lett. **117**, 016602 (2016).
[29] T. Liang, Q. Gibson, M. N. Ali, M. Liu, R. J. Cava, and N. P. Ong, Nat. Mater. **14**, 280 (2014).
[30] B. Q. Lv, H. M. Weng, B. B. Fu, X. P. Wang, H. Miao, J. Ma, P. Richard, X. C. Huang, L. X. Zhao, G. F. Chen, Z. Fang, X. Dai, T. Qian, and H. Ding, Phys. Rev. X **5**, 031013 (2015).
[31] S. Borisenko *et al.*, Phys. Rev. Lett. **113**, 027603 (2014).
[32] Amit and Y. Singh, Phys. Rev. B **97**, 054515 (2018).
[33] J. Gooth *et al.*, Nature (London) **547**, 324 (2017).
[34] J. Hu, Z. Tang, J. Liu, Y. Zhu, J. Wei, and Z. Mao, Phys. Rev. B **96**, 045127 (2017).
[35] K. Zhao, E. Golias, Q. H. Zhang, M. Krivenkov, A. Jesche, L. Gu, O. Rader, I. I. Mazin, and P. Gegenwart, Phys. Rev. B **97**, 115166 (2018).
[36] S. Huang, J. Kim, W. A. Shelton, E. W. Plummer, and R. Jin, Proc. Natl. Acad. Sci. USA **114**, 6256 (2017).
[37] J. Hu, Y. Zhu, X. Gui, D. Graf, Z. Tang, W. Xie, and Z. Mao, Phys. Rev. B **97**, 155101 (2018).
[38] W. Zheng, R. Schoenemann, N. Aryal, Q. Zhou, D. Rhodes, Y.-C. Chiu, K.-W. Chen, E. Kampert, T. Forster, T. J. Martin, G. T. McCandless, J. Y. Chan, E. Manousakis, and L. Balicas, Phys. Rev. B **97**, 235154 (2018).